J. Plasma Physics (2000), *vol.* 64, *part* 4, *pp.* 489–506. Printed in the United Kingdom
© 2000 Cambridge University Press

Parametric interactions inside a magnetron

D. J. KAUP,[1] J. O. EL-REEDY[2] and GARY E. THOMAS[3]

[1]Institute for Nonlinear Studies and Departments of Physics and Mathematics, Clarkson University, Potsdam, NY 13699-5815, USA

[2]Department of Physics, Clarkson University, Potsdam, NY 13699-5815

[3]Communications & Power Industries, 150 Sohier Road, Beverly, MA 01915, USA

(Received 16 November 1999 and in revised form 1 May 2000)

Abstract. The purpose of this work is to understand theoretically what are the possible noise levels in a magnetron or a crossed-field amplifier (CFA), due to parametric three-wave interactions in the electron plasma, at various operating parameters. Our approach is to use the cold-fluid equations and their Fourier decomposition into a background (DC) mode, a pump (RF) mode, and two other noise (RF) modes. The two RF noise modes are assumed to interact parametrically with the large RF pump mode, and to satisfy the standard resonance conditions for the sum of the wave vectors and sum of the frequencies. We use our previous results to determine the background mode and the RF pump mode. Any strong RF electric field propagating in a crossed-field electron vacuum device can drive a Brillouin sheath unstable by means of a Rayleigh instability, whenever a wave–particle resonance can be found inside the sheath. What happens physically is that, at the resonance, the laminar flow of the electrons is strongly disturbed, and a diffusion process ensues, whereby the electrons diffuse away from the resonance region. This upsets the balance in the Brillouin flow, causing the electrons to redistribute into a new average DC density profile – which may be far from the original Brillouin profile, but is a stationary solution of a nonlinear diffusion equation. Using these stationary density profiles, we can then study the propagation of small RF signals on such a DC background, as well as their parametric interactions with the RF pump wave, at various DC voltages and magnetic fields. In addition to being able to predict the operating regime and the DC current flow, these studies demonstrate that parametric interactions probably limit the operating voltage range of a typical magnetron or crossed-field amplifier to about 20% above the Hartree voltage.

Dedication

This paper is dedicated to John Dougherty on the occasion of his 65th birthday.

1. Introduction

The purpose of this work is to investigate the theoretical consequences that can be drawn from the mathematical modelling of a crossed-field vacuum device, such as a crossed-field amplifier (CFA) or a magnetron. These devices have been analysed with PIC codes (Palevski et al. 1981; Dombrowski 1988; Riyopoulos 1993) and guiding-centre theory (Davidson 1984; Riyopoulos 1996; and references therein).

https://doi.org/10.1017/S0022377800008783 Published online by Cambridge University Press

Our approach has been to use Fourier modes. The justification for this has been the fact that these devices, when adjusted and operating properly, do oscillate in a single mode. Thus their single-mode operation should be describable by an expansion in Fourier modes. The original Fourier multiscale expansion for a planar model of these devices was first described in Kaup and Thomas (1989), and the importance of the second-order (quasilinear) conditions for determining the operating electron density profiles was detailed in Kaup and Thomas (1996, 1997). It was then demonstrated in Kaup and Thomas (1998) that this model did indeed produce reasonable predictions for the phase shifts, DC current flow, and other characteristics of these devices. Furthermore, when the total density was reconstructed from the two main Fourier components (the main RF wave and the DC background), the resulting density profiles were very similar to those seen in numerical simulations, showing even the standard spoke structure (see Fig. 4).

The dominant interaction in such a crossed-field device is the wave–particle interaction (diocotron). This interaction drives the classical Brillouin flow (Brillouin 1945) nonlinearly unstable (Kaup and Thomas 1996) in the presence of high-frequency (RF) waves, propagating in the slow-wave structures that these devices contain. The instability initializes as a linear wave–particle instability in a Rayleigh-like equation with a shear flow. Once this linear instability initializes, it will trigger the nonlinear instability, which is a consequence of second-order (quasilinear) theory (Davidson 1985; Davidson and Tang 1985; Kaup and Thomas 1989). The growth rate of this nonlinear instability is directly proportional to the density gradient at the edge of the sheath (Kaup and Thomas 1996), which, for a Brillouin flow, is very large. The second-order theory then predicts that the electron density will change and evolve into a new density profile – one that will be in equilibrium with the propagating RF wave. This profile will consist of an oscillating background, on top of which is a series of periodic 'spokes'. These spokes extend from the sheath up to the anode, and carry the DC current from the cathode to the anode. The physics of the turn-on process for developing these spokes has been described in Kaup and Thomas (1998).

Here, we shall extend these results to include the small-signal response and three-wave parametric interactions. Once the above operating density profile has been achieved, the RF wave grows until it saturates. Now it can no longer be considered to be infinitesimal, and, owing to nonlinear terms in the cold-fluid equations, the main RF wave will beat against any other RF waves (noise) in the device, which will then generate all possible harmonics and beat waves. To study this, we need, and shall develop here, the small-signal response for these noise modes, their dispersion characteristics, their modal profiles, and their energy characteristics. We then allow these waves to beat against the main RF wave (the pump), and determine their nonlinear growth characteristics. As we shall see, for operating voltages only slightly above the Hartree voltage, the nonlinear growth rates of these noise modes are small. However, as one goes up to about 20% above the Hartree voltage, the nonlinear growth rate of these modes suddenly and rapidly increases. In such circumstances, the noise modes would then rapidly grow and interfere with the operation of the device. This is perhaps the explanation for what is observed experimentally. This then suggests that there is indeed a limit to the operating voltages of these devices, well below the Hull (cutoff) voltage, and that this limit is imposed by parametric interactions.

In Sec. 2, we review the major equations from our previous studies. Then, in

https://doi.org/10.1017/S0022377800008783 Published online by Cambridge University Press

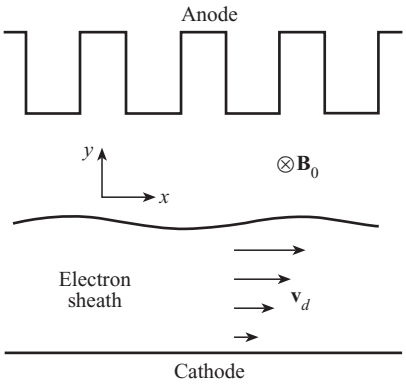


Figure 1. The geometry and configuration of a planar magnetron or CFA. The magnetic field is directed into the paper and the electron drift velocity is to the right. The z axis is perpendicular to the paper, the x axis is parallel to the cathode surface, and the y axis is perpendicular to the cathode.

Sec. 3, we present the small-signal characteristics of a model of the CPI T266 CFA, which has been found to operate in an ultralow-noise regime. In Sec. 4, we consider the theory of the three-wave interaction in this device, and present the expressions for the coupling coefficients and other parameters of the three-wave equations. We then use the small-signal characteristics to evaluate the nonlinear parametric growth rate of these modes in Sec. 5. In Sec. 6, we discuss our results.

2. Basic equations

The geometry and configuration that we shall be using is shown in Fig. 1, which is a diagram of a 'planar magnetron'. A planar geometry is preferred for analytical treatment because of its simplicity. Although actual devices are usually cylindrical, the essential physics are contained in the planar model. At the bottom is the cathode, which is an electron-emitting material. It is located in the (x, z)-plane and at $y = 0$. We take the ambient magnetic field to be along the negative z axis, so that the electron drift velocity will be in the positive x direction. The electron cyclotron frequency is $\mathbf{\Omega} = eB_0/mc$, where B_0 is the ambient magnetic field. Next to the cathode is the electron sheath, which extends out for some distance from the cathode. The anode is located at a distance l above the cathode. On the anode, is a slow-wave structure, which is simply a wave guide, along which the RF wave will propagate. This slow-wave structure is there to (i) slow down the electromagnetic RF wave, which is moving near the speed of light inside the anode structure, and (ii) to select the effective RF (electrostatic) wave vector k that the plasma will see and will respond to.

The basic cold-fluid equations describing this physical system are

$$\partial_t n + \boldsymbol{\nabla} \cdot (\mathbf{v}n) = 0, \tag{1}$$

$$\partial_t \mathbf{v} + (\mathbf{v} \cdot \boldsymbol{\nabla})\mathbf{v} - \boldsymbol{\nabla}\phi + \mathbf{v} \times \mathbf{\Omega} = 0, \tag{2}$$

$$\nabla^2 \phi = n. \tag{3}$$

In the above equations, the fluid velocity vector is in the (x, y) plane and all quantities are taken to be independent of the z coordinate. We have also simplified the notation by taking n to be the electron plasma frequency squared ($4\pi e^2 \rho/m$, where

https://doi.org/10.1017/S0022377800008783 Published online by Cambridge University Press

e and m are the electron charge and mass and ρ is the electron number density) and ϕ to be e/m times the electrostatic potential. We shall use this notation in the remainder of the paper.

These equations (1)–(3) are then expanded in Fourier components of $e^{i(kx-\omega t)}$ (Kaup and Thomas 1996). On the fast time scale, the DC Fourier component of this expansion gives the 'background solution', which satisfies

$$\mathbf{v} = v_0(y)\hat{\mathbf{x}}, \tag{4}$$

$$v_0(y) = \frac{\partial_y \phi_0(y)}{\mathbf{\Omega}}, \tag{5}$$

where ϕ_0 is obtained from Poisson's equation

$$\partial_y^2 \phi_0 = n_0\,, \qquad \phi_0(0) = 0 = \partial_y \phi_0(0), \tag{6}$$

and where we have taken the background potential ϕ_0 to be zero at the cathode ($y = 0$) and have imposed the space-charge-limited current condition $\partial_y \phi_0(0) = 0$. Thus, from (6), the solution for $\phi_0(y)$ is determined once $n_0(y)$ is given. On this fast time scale, the background electron density profile $n_0(y)$ is arbitrary, except that it does have to satisfy one integral condition, namely, that the potential at the anode, $\phi_0(y = l)$, must equal the applied cathode–anode DC voltage V_0. Also, if the background electron density profile is to be linearly stable, then it is necessary for the density profile to always have a non-positive density gradient (Davidson 1985).

Next we consider the fast time scale of the fundamental Fourier components of these equations, in the presence of the above background. These can be reduced to (Buneman et al. 1966; Kaup and Thomas 1989):

$$\partial_y p = Au, \tag{7}$$

$$\partial_y u = Bp, \tag{8}$$

where

$$A = \mathbf{\Omega}^2 - \omega_e^2, \tag{9}$$

$$B = \frac{k^2}{A} - \frac{k\partial_y n_0}{\mathbf{\Omega}\omega_e A} - \frac{2k^2 n_0 \mathbf{\Delta}^2}{\mathbf{\Omega}^2 A^2}, \tag{10}$$

$$u = -ikv_{1x}, \tag{11}$$

$$p = Av_{1y}, \tag{12}$$

$$\omega_e = \omega - kv_0, \tag{13}$$

$$\mathbf{\Delta}^2 = \mathbf{\Omega}^2 - n_0. \tag{14}$$

In the above, ω_e is the frequency of the RF wave as seen by the electrons moving at the background drift velocity $v_0(y)$, and $\mathbf{\Delta}$ is the local orbital oscillating frequency for individual particle orbits (Prasad et al. 1987; Kaup and Thomas 1992), which would vanish for a Brillouin flow. In (11) and (12), v_{1x} and v_{1y} are the x and y components of the perturbed velocity fields. The perturbed electrostatic potential ϕ_1, its gradient $\partial_y \phi_1$, and the perturbed electron density n_1, are obtained from p and u as follows (Kaup and Thomas 1989).

$$n_1 = ip\left(\frac{2kn_0^2}{\mathbf{\Omega}A^2} - \frac{\partial_y n_0}{A\omega_e}\right), \tag{15}$$

https://doi.org/10.1017/S0022377800008783 Published online by Cambridge University Press

$$\phi_1 = \frac{ip\Delta^2}{Ak\Omega} - \frac{iu\omega_e}{k^2}, \tag{16}$$

$$\partial_y \phi_1 = \frac{i\Omega}{k} u - \frac{i\omega_e}{A} p. \tag{17}$$

The boundary conditions on (7) and (8) follow from the boundary conditions on ϕ_1. At the cathode, which is grounded, the perturbed potential must vanish. Thus $\phi_1(y = 0) = 0$. Then, by (16), one has the ratio of u to p at $y = 0$ determined. This has now determined the solution up to an overall magnitude.

One must still match this solution in the cathode–anode region to the solution inside the slow-wave structure. This is done by using a model of the logarithmic derivative for the slow-wave structure, $1/\mu_{\text{sws}}(k, \omega)$, where

$$\mu = \frac{d\phi_1}{dy} \frac{1}{k\phi_1}\bigg|_{y=l}.$$

Note that μ can, in general, be computed directly from the slow-wave structure, without any knowledge about the interior solution. In general, the interior solution will match to the value of μ_{sws}, only for selected values of k and $\gamma\,(= \text{Im}(\omega))$ when the value of the real part of ω is fixed. The values of k and γ at which a match does occur will be called 'eigenvalues'. The modal structure, $p(y)$ and $u(y)$, at these eigenvalues will be called the 'eigenmode' of these equations. For any eigenmode, its magnitude can be normalized so that the value of E_x at the vane tips of the slow-wave structure has a given fixed value E_{xa}. For definiteness, we shall denote the RF operating frequency by ω_0 when needed.

As we look at slower time scales, the next order is where the RF waves beat against themselves. Owing to the nonlinear terms in (1)–(3), this beating forces the DC solution to slowly evolve away from its initial solution, with several of the DC quantities becoming shifted, proportional to the square of the RF amplitude. An analysis of all such shifts was given in Davidson (1985) and Kaup and Thomas (1989). There, it was also shown that the background potential (and the background density profile) will evolve according to

$$\partial_\tau \partial_y \phi_0 - C_2 \Delta^2 = D \partial_y n_0, \tag{18}$$

where C_2 is a constant of integration, τ is a slow time variable, and

$$D = \frac{2\gamma p^* p}{\omega_e^* \omega_e A^* A} e^{2\gamma t}, \tag{19}$$

which is the nonlinear diffusion coefficient. In (19), γ is the growth rate of the pump RF mode, which is the imaginary part of the RF frequency ω. It is this equation that determines the stationary profiles of the electron density. To find them, one uses the adiabatic approximation and requires $\partial_\tau n_0$ to vanish, and n_0 to vanish at the anode. It can be shown that we then have (Kaup and Thomas 1996, 1998)

$$n_0 = \Omega^2 (1 - e^{-\theta}), \tag{20}$$

where

$$\theta = C_2 \int_y^l \frac{dy}{D}, \tag{21}$$

which defines the stationary density profile in terms of the nonlinear diffusion coefficient and the constant C_2. The constant C_2 is then determined by requiring

https://doi.org/10.1017/S0022377800008783 Published online by Cambridge University Press

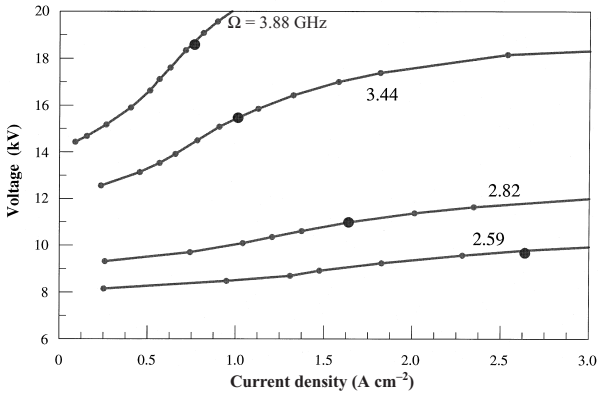


Figure 2. Predicted operating voltage for the CPI T266 device versus current density for selected ambient magnetic fields at a fixed RF pump frequency of 3.1 Ghz. The large solid circles on the curves label the voltage above which the parametric growth rate dominates over the linear growth rate (see Sec. 5).

the DC electrostatic potential ϕ_0, obtained by integrating Poisson's equation, to be exactly equal to the applied DC voltage V_0 (Kaup and Thomas 1998) at the anode. Further, we have that C_2 is directly related to the asymptotic DC current density (Kaup and Thomas 1997),

$$J_{2y} = C_2 \Omega^2 \,, \tag{22}$$

and represents a constant, uniform, vertical particle flux. There are two contributions to this DC current. The first is the DC average of the RF density variations n_1, beating against the RF vertical velocity v_{1y}. The second is the DC average of the x component of the convective derivative in Newton's equation, which generates a second-order DC vertical drift velocity v_{2y}. The sum of these two contributions can be shown (Kaup and Thomas 1997) to be the constant amount given in (22). Naturally, the vertical current density has to be some constant value, such as this, since the density profile is stationary. Its source is the ideal cathode, which emits and absorbs electrons on demand, maintaining the space-charge-limited-current condition, (6), and providing a constant potential surface. Its sink is the anode.

One may solve these coupled equations, (7), (8), (19), and (20), in an iterative fashion until the solution converges to a stable solution (Kaup and Thomas 1998). Thus, given the ambient magnetic field, $\mathbf{\Omega}$, the applied DC voltage, V_0, the anode–cathode spacing l, and a model for the μ of the slow-wave structure, $\mu_{\rm sws}(k)$, we can then determine the pump RF eigenmode $[p(y), u(y)]$ and the eigenvalues $[k, \gamma]$, the stationary density profile $n_0(y)$, and the DC current density, $C_2/\mathbf{\Omega}^2$ for an operating device.

As an example of the data obtainable, we show in Fig. 2 the theoretical operating range for the CPI T266 device, where we have plotted the relative applied voltage (V_r = actual voltage/cutoff voltage; the cutoff voltage is the same as the Hull voltage $= e\mathbf{\Omega}^2 l^2/2m$) versus the current density J_y for various magnetic fields at a fixed RF frequency of 3.1 Ghz. These curves are quite similar to typical experimental curves of this device, and other similar devices. In Fig. 3 we show the background density profiles $n_0(y)$ at various relative voltages (defined above) for a typical case where $\omega = 0.90\mathbf{\Omega}$. For these parameters, the Hartree voltage is $V_r = 0.62$ (which is determined from Fig. 2, in the limit of zero current). Note that the lowest operating

https://doi.org/10.1017/S0022377800008783 Published online by Cambridge University Press

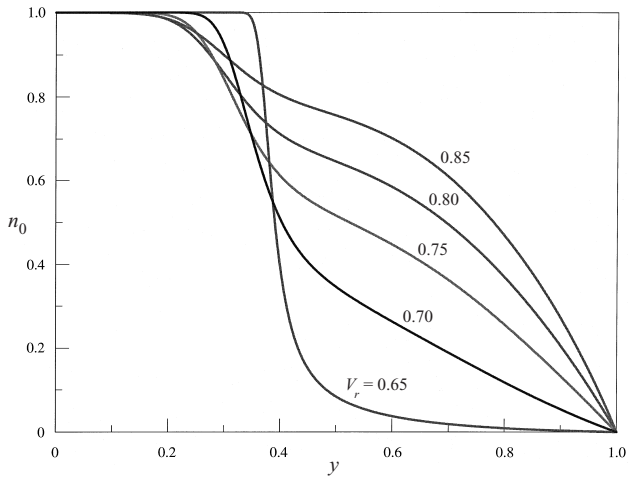


Figure 3. Stationary density profiles (in units of $\mathbf{\Omega}^2$) as a function of the operating voltage, for a pump RF frequency of 3.1 GHz and a magnetic field of 3.44 GHz ($\omega = 0.90\mathbf{\Omega}$). V_r is the operating voltage, in units of the Hull cutoff voltage. At $V_r = 0.65$, which is just above the Hartree voltage of $V_r = 0.62$ at these parameters, the tube has just started to operate. Note the distinct Brillouin structure at this voltage, to which is attached a weak, but distinct, foot structure.

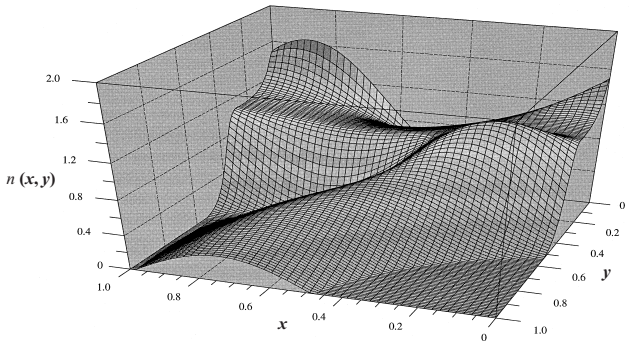


Figure 4. Plot of $n(x, y)$ versus x and y for one period of the propagating RF wave, and for $V_r = 0.70$ and $\omega = 0.90\mathbf{\Omega}$. Note the structure in the foreground, which is the spoke of charge, reaching up to the anode and carrying the DC current. Here, since $\omega_0 < \mathbf{\Omega}$, there is no cyclotron resonance inside the device. However, one can also still a disturbance in the background, just above the cathode, due to the proximity of the lower cyclotron resonance in phase space.

voltage shown, $V_r = 0.65$, is just above the Hartree voltage, and that here the profile shape is very Brillouin-like, but it does have a very weak foot-like ramp, extending up to the anode. As the relative voltage goes up, this foot-like structure becomes more and more distinct. At $V_r = 0.75$, the shape of the density profile has definitely became non-Brillouin, with the additional structure beginning to occupy a larger share of the vacuum region. This is also just below the point where the parametric interactions and the nonlinear growth rate are starting to dominate, as we shall see later. As a consequence, the operating voltages above $V_r = 0.75$ are probably experimentally inaccessible.

In Fig. 4, we have plotted the total electron density $n(x, y)$ (background plus

https://doi.org/10.1017/S0022377800008783 Published online by Cambridge University Press

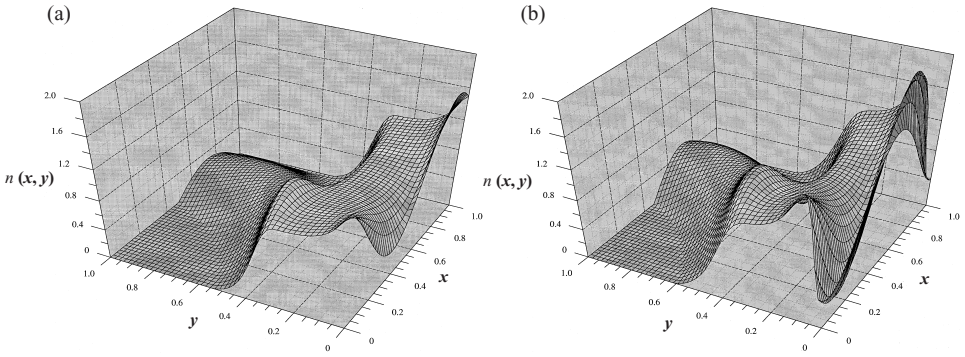


Figure 5. Comparison of the stationary density profiles when the RF pump frequency ω_0 is below, and then above, the cyclotron frequency. Each operating voltage was chosen to be about 12% above the respective Hartree voltage. (a) is a view of Fig. 4 from the back side. Here the oscillations near the cathode due to the proximity of the lower cyclotron resonance in phase space can be more clearly seen. In (b), we have the same RF frequency, but a smaller magnetic field, $\omega_0 = 1.10\Omega$, and a Hartree voltage of $V_r = 0.70$. The operating voltage, $V_r = 0.78$, is higher, so as to maintain an equivalent ratio to the Hartree voltage. Here one can see that the lower cyclotron resonance ($\omega_e = \Omega$) does occur inside the device, and very near the cathode, where there are very strong variations in the electron density.

the RF mode) versus x and y for one period of the propagating RF wave, and for the $V_r = 0.70$ density profile from Fig. 3, assuming that the RF pump has saturated. Note the structure in the foreground, which is the spoke of charge, reaching up to the anode and carrying the DC current. The strong oscillation seen at the back and deep in the sheath is due to the proximity of the lower 'magnetron' or cyclotron resonance. The cyclotron resonances are where $\omega_e = \pm\Omega$. The lower (upper) cyclotron resonance is where $\omega_e = +\Omega$ ($\omega_e = -\Omega$), and when it occurs inside the physical region, it occurs near the cathode (anode). However, since here $\omega_0 < \Omega$, where ω_0 is the pump RF frequency, this resonance does not occur inside the physical region, and one is only seeing a disturbance due its close proximity in phase space.

Now let us consider the case where $\omega_0 > \Omega$, which is the approximate parameter regime where the CPI T266 operates in an ultralow-noise mode. In this regime, the shape of the background density profiles still look essentially the same as in Fig. 3, except that the Hartree voltage will have been shifted. However, there is a definite change in the structure of the RF modes, since now the lower cyclotron resonance ($\omega_e = \Omega$) does occur in the physical region. There are obvious enhancements seen to occur in the RF quantities at the position of the lower cyclotron resonance, as is seen in Fig. 5(b). For comparison, we show in Fig. 5(a) the back view of Fig. 4, which is when the lower cyclotron resonance is outside the physical region. In Fig. 5(b), we show the same view when the lower cyclotron resonance occurs inside the physical region of the device. Here we have taken the operating voltages to be about 12% above the respective Hartree voltages and the RF frequencies to be equal. In Fig. 5(b), we have a weaker magnetic field, where $\omega_0 = 1.10\Omega$, and one sees a very distinct and large structure inside the density, deep in the sheath and near the cathode. Some of the effects of this can be made more obvious if one plots the RF velocity fields for these solutions.

In Fig. 6, we show the velocity fields of the RF pump for solutions close to those

https://doi.org/10.1017/S0022377800008783 Published online by Cambridge University Press

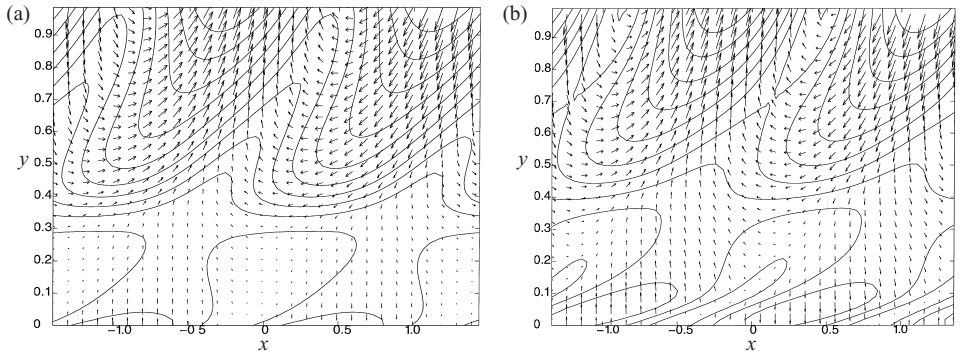


Figure 6. Plots of the velocity fields versus x and y for one period of the propagating RF wave for the solutions near those shown in Fig. 5. In (a), we show the typical case when $\omega_0 < \Omega$, and the lower cyclotron resonance lies outside the physical region (corresponding to Figs. 4 and 5a). In (b), we have a weaker magnetic field, $\omega_0 > \Omega$, and now the lower cyclotron resonance lies inside the physical region. Note that when the resonance is inside the physical region, the electrons in the sheath and near the cathode are much more energetic than in the other case.

in Fig. 5. Figure 6(a) corresponds exactly to Fig. 5(a) (13.3% above the Hartree voltage), while Fig. 6(b) almost corresponds to Fig. 5(b). The difference is only one of operating voltage: Fig. 5(b) is at $V_r = 0.78$ (10.8% above Hartree) while Fig. 6(b) is at $V_r = 0.80$ (13.7% above Hartree). A key difference between these two plots is that inside the sheath, and near the cathode, the velocity fields are stronger and more intense in Fig. 6(b) than in Fig. 6(a), which is where the lower cyclotron resonance is. In fact, the RF velocity field at the cathode, for $\omega_0/\Omega = 0.90$ and 13.3% above Hartree, is roughly equal to that at $\omega_0/\Omega = 1.10$, which is only 6.0% above Hartree. The point is that, for $\omega_0/\Omega > 1$, there is addition turbulent motion at the cathode.

This additional turbulent motion in Fig. 6(b) does seem to be directly related to the presence of the lower cyclotron resonance. Certainly, electrons striking the cathode surface in Fig. 6(b) will strike it with more velocity and energy, and would thereby generate more secondary electrons. This is also the regime where the T266 device operates in an ultralow-noise mode. We note that it has been suggested that cathode emission could play a role in the ultralow-noise phenomena. What we see here is consistent with that – in that an increased activity of the electrons near the cathode is indeed being seen.

3. Small-signal response

As outlined above, we can determine the nonlinear stationary operating state of a CFA. Now we turn our attention to describing what noise modes could possibly be present, and what their properties are. These results will be key results for our later analysis of parametric interactions.

3.1. Dispersion curves

The noise modes will satisfy exactly the same equations as the RF pump, namely (7)–(17). Each of these modes can be labeled by its k value. The real and imaginary parts of the frequency will be determined by matching these solutions to the slow-

https://doi.org/10.1017/S0022377800008783 Published online by Cambridge University Press

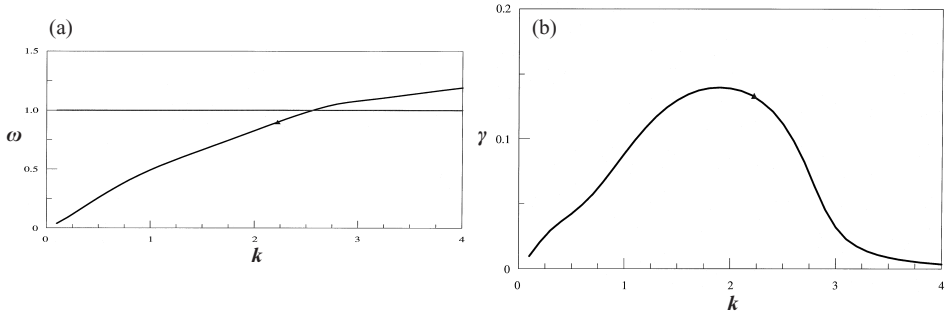


Figure 7. The linear dispersion characteristics for small signals on the density profile in Fig. 3 ($\omega_0/\Omega = 0.90$) for the operating voltage of $V_r = 0.70$ (shown also in Fig. 4). (a) The frequency curve $\omega(k)$ in units of the cyclotron frequency. (b) The linear growth-rate curve $\gamma(k)$, also in units of the cyclotron frequency. The units of k are $1/l$. The triangles indicate the RF pump values at $k_0 = 2.23$.

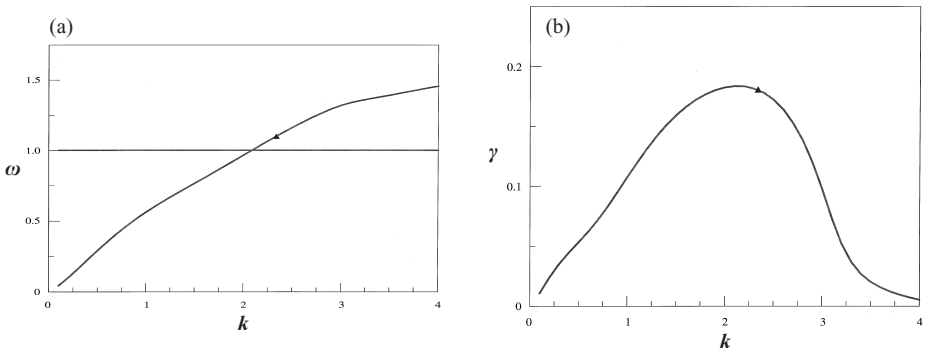


Figure 8. The linear dispersion characteristics for small signals on the density profile when $V_r = 0.72$ and $\omega_0/\Omega = 1.10$. (a) The frequency curve $\omega(k)$ in units of the cyclotron frequency. (b) The linear growth-rate curve $\gamma(k)$, also in units of the cyclotron frequency. The units of k are $1/l$. The triangles indicate the RF pump values at $k_0 = 2.34$.

wave structure. These are a function of k, giving us the two curves $\omega(k)$ and $\gamma(k)$. We shall refer to these curves as the 'dispersion curves' for small-signal response.

In Fig. 7, we show a typical set of such dispersion curves for a background density profile near that of Fig. 4 ($V_r = 0.70$, $\omega = 0.90\Omega$). The triangles indicate the operating point for the RF pump. The $\omega(k)$ curve is typical, consisting of more or less piecewise-linear segments, with a slight overall negative curvature, and with a more or less distinct break in the slope, at a frequency near the cyclotron frequency (note that $\omega(k)$ is given in units of the cyclotron frequency). The growth-rate curve given in Fig. 7(b) is also typical. What is uniformly observed is that the growth rate at the operating point is almost the largest rate present, and above that point, the growth rate then rapidly decreases. For values of k below the operating point, the growth rate tends to be more or less linear in k. In Fig. 8, we show the corresponding results for $\omega_0/\Omega = 1.10$.

Among the most important influences on the growth rate, and on the flow patterns, are the relative locations of the diocotron (wave–particle) and cyclotron resonances. In Fig. 9, we plot the positions of the diocotron resonance, y_0, and the lower cyclotron resonance, y_-, as functions of k (the upper cyclotron resonance occurs at higher k values and is outside the physical region). In Fig. 9(a), we show the

https://doi.org/10.1017/S0022377800008783 Published online by Cambridge University Press

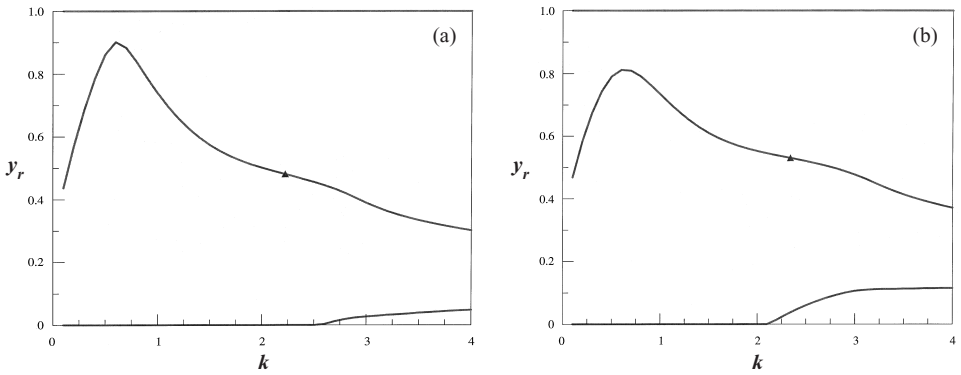


Figure 9. The positions of the diocotron resonances y_0, and the lower cyclotron resonance, y_- as functions of the small-signal wavevector k for the background densities (a) $\omega_0/\Omega = 0.90$, $V_r = 0.72$ and (b) $\omega_0/\Omega = 1.10$, $V_r = 0.80$.

case when the cyclotron frequency is larger than the RF frequency ($\omega_0/\Omega = 0.90$ and $V_r = 0.72$), and in Fig. 9(b), we show the other case where ($\omega_0/\Omega = 1.10$ and $V_r = 0.80$). An important difference is the location of the appearance of the lower cyclotron resonance in relation to the operating point. For $\omega_0/\Omega > 1$, the lower cyclotron resonance starts below the operating point, and for $\omega_0/\Omega < 1$, it starts above the operating point.

The upper cyclotron resonance ($\omega_e = -\Omega$; enters from the anode), seems to be of a lesser importance, and is not seen in the physical region until k is much higher than the range in Fig. 9. However, when k becomes sufficiently large that this resonance also appears in the physical regime, we see a steep drop in the already small growth rate.

3.2. Modal energy density

Another interesting characteristic of the small-signal modes is the modal energy as a function of the operating voltage. From the cold-fluid equations, we have the conservation law

$$\partial_t \mathscr{E} + \boldsymbol{\nabla} \cdot \mathbf{G} = 0\,, \tag{23}$$

where

$$\mathscr{E} = \tfrac{1}{2} n v^2 + \tfrac{1}{2} |\boldsymbol{\nabla}\phi|^2\,, \tag{24}$$

$$\mathbf{G} = \tfrac{1}{2} n v^2 \mathbf{v} - n\phi\mathbf{v} - \phi\boldsymbol{\nabla}\partial_t\phi\,. \tag{25}$$

Obviously, we can interpret $\mathscr{E}$ as the energy density. To obtain the modal energy of the small-signal modes, one has to expand (23) about the background and the RF pump wave, carrying out the expansion to second order in the small-signal amplitude. The purpose of the calculation is to determine how much the addition of one of these modes to the system will change the energy density of the system. Ignoring the interactions between the RF pump and the noise modes, one obtains for the second-order time average (DC) of (24),

$$\begin{aligned}\mathscr{E}_2 = {} & n_0(v_0 v_{2x} + |v_{1y}|^2 + |v_{1x}|^2) + v_0(\tfrac{1}{2} n_2 v_0 + n_1 v_{1x}^* + n_1^* v_{1x}) \\ & + \partial_y\phi_0\partial_y\phi_2 + |\partial_y\phi_1|^2 + k^2|\phi_1|^2\,,\end{aligned} \tag{26}$$

where subscript 2 indicates a second-order, DC quantity. Expressions for v_{2x} and ϕ_2 are found in Kaup and Thomas (1989), where ϕ_2 is obtained from Poisson's

https://doi.org/10.1017/S0022377800008783 Published online by Cambridge University Press

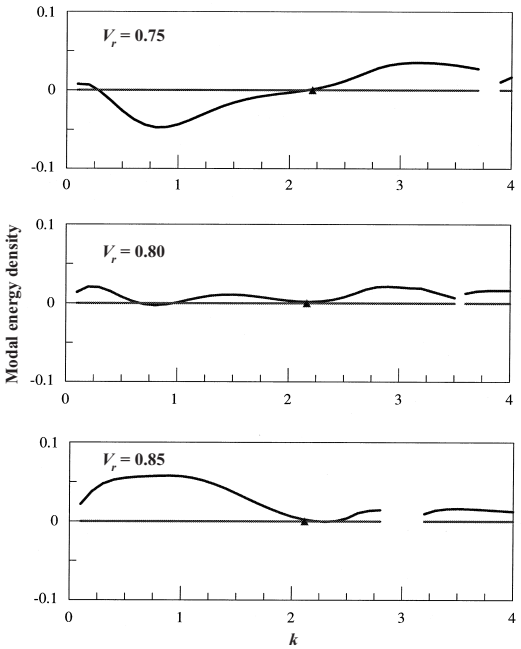


Figure 10. The modal energy density as a function of k for three voltages $V_r = 0.75$, 0.80 and 0.85, for $\omega_0/\Omega = 0.90$. The gaps in the curves are where the upper cyclotron resonance crosses the anode, into the physical region, and are more difficult to evaluate numerically.

equation:

$$\partial_y^2 \phi_2 = n_2 \,, \qquad \phi_2(0) = 0 = \partial_y \phi_2(0) = \phi(l) \,, \tag{27}$$

while v_{2x} is given by

$$v_{2x} = \frac{1}{\Omega} \partial_y \phi_2 - \frac{1}{\Omega |p|^2} \partial_y \left(\frac{|p|^4}{|A|^2} \right) . \tag{28}$$

n_2 will be obtained from the variation of (20). Physically, if we have a noise mode present, it does contribute to the ponderomotive force on the electrons, and must be considered. Thus there will be an additional contribution to the nonlinear diffusion coefficient, over and beyond what the pump RF mode contributes. Varying (20) then gives

$$n_2 = \delta n = \Omega^2 e^{-\theta} \delta\theta \,, \tag{29}$$

where

$$\delta\theta = \frac{\delta C_2}{C_2} \theta - \int_y^l \frac{C_2}{D^2} \delta D \, dy \,. \tag{30}$$

δC_2 is the shift in the coefficient C_2 due to the noise mode being present. This shift will be determined by the condition $\phi_2(l) = 0$, since the anode–cathode voltage is fixed. The shift in the nonlinear diffusion coefficient is simply due to the increase in the ponderomotive force on the electrons, which is

$$\delta D = \left(\frac{2\gamma |p|^2}{|\omega_e|^2 |A|^2} \right)_{\text{noise}} , \tag{31}$$

where the subscript 'noise' means that γ, ω_e, A, and p in the above are to be evaluated for the noise mode, according to the values given by $\omega(k)$ and $\gamma(k)$.

https://doi.org/10.1017/S0022377800008783 Published online by Cambridge University Press

In Fig. 10, we show a typical result for the modal energy density as a function of k for a series of operating voltages V_0, for $\omega_0/\Omega = 0.90$. What one observes here is that for voltages close to the Hartree voltage, these modal energies are typically negative for wavenumbers below the RF pump, and are typically positive for wavenumbers above that of the RF pump. This means that in order to create these modes, no energy is required. Rather, any increase in their amplitude will result in energy being given up to the system. As the operating voltage rises, the negative energy values slowly, and more or less uniformly, become positive. They usually do not vanish until above or near that voltage at which the nonlinear growth rate dominates.

How important these negative energy densities are is not known. We have observed them for several parameter regimes, and the above results are typical of what was found.

4. Three-wave interactions

As the amplitude of any noise mode grows linearly, eventually it will become sufficiently large that three-wave parametric interactions with the other modes will become important. The three-wave interaction is a resonant interaction, in which the sums of two of the wavevectors and frequencies are equal to those of the third wave. By considering complex conjugates, and allowing the wavevectors and frequencies to have negative values, one can always express this resonance in the form

$$k_1 + k_2 + k_3 = 0\,, \tag{32}$$

$$\omega_r(k_1) + \omega_r(k_2) + \omega_r(k_3) = \epsilon\delta\omega_r\,, \tag{33}$$

where the ks are the three wavevectors, $\omega_r(k)$ is the real part of the linear dispersion curve from the previous section, and ϵ is an expansion parameter. The quantity $\delta\omega_r$ is the frequency mismatch, which will be a function of two of the wavevectors. The size of this mismatch will strongly affect the nonlinear growth rate.

Let us briefly outline the derivation of the equations for the evolution of the amplitudes of the three-wave interaction. To obtain these equations, we start with an expansion of the form

$$\begin{aligned} n = n_0 &+ \epsilon\psi_1[n_1(y)e^{i(k_1x-\omega_{r,1}t)} + \text{c.c.}] + \epsilon\psi_2[n_2(y)e^{i(k_2x-\omega_{r,2}t)}e^{\gamma_2 t} + \text{c.c.}] \\ &+\epsilon\psi_3[n_3(y)e^{i(k_3x-\omega_{r,3}t)}e^{\gamma_3 t} + \text{c.c.}] + \ldots\,, \end{aligned} \tag{34}$$

where ϵ is our expansion parameter, and $\omega_{r,1} = \omega_r(k_1)$, $\gamma_1 = \gamma(k_1)$, etc. are the real and imaginary parts of the generalized frequency. $\psi_j(\chi,\tau)$ is the envelope of the amplitude of the jth wave, the subscripts now designate which wave, and 'c.c.' stands for the complex conjugate of the preceding term. Note how the dependences on the coordinates have been separated. The y dependence is only found in the n_j. This, along with the usual plane-wave dependence of x and t, defines the fast-scale variations in the solution. All nonlinear parametric interactions occur on the slower scale where $\chi = \epsilon x$ and $\tau = \epsilon t$. Thus what we have is a set of non-interacting modes on the fast scale, but if we follow these modes over a longer spatial and/or time scale, we shall see these modes interact and their amplitudes and phases change.

Using (34), and similar expansions for $\boldsymbol{v}$, and ϕ, one expands the cold-fluid equations, retaining only terms of order ϵ^2. Major details are given in the Appendix. A Macsyma notebook† was used to perform the detailed calculations and to obtain

† Symbolic computational software, MACSYMA, Version 2.2 (obtainable from Macsyma Inc., 20 Academy Street, Arlington, MA 02174-6436, USA).

https://doi.org/10.1017/S0022377800008783 Published online by Cambridge University Press

the coefficients and equations given below, as well as the Fortran statements used in the numerical calculations. What is obtained are the evolution equations for the ψs. These are

$$C_{\tau,j}\partial_\tau\psi_j + C_{\chi,j}\partial_\chi\psi_j = -C_{3w,j}\psi_k^*\psi_l^* e^{i\delta\omega_r\tau}e^{\delta\gamma_j\tau}\,, \tag{35}$$

where j, k, and l can be any permutation of (1, 2, 3) and

$$\delta\gamma_j = \frac{\gamma_k + \gamma_l - \gamma_j}{\epsilon}\,. \tag{36}$$

The expressions for the coefficients are

$$\begin{aligned} C_{\tau,j} = {} & \frac{k_j}{\Omega}\int_0^l \frac{p_j}{A_j}\left[2n_0u_j\left(2\frac{\omega_{e,j}^2}{A_j}+1\right) - 4\Delta^2 n_0\frac{k_jp_j\omega_{e,j}}{\Omega A_j^2} + \frac{k_jp_j}{\omega_{e,j}^2}\frac{dn_0}{dy}\right]dy \\ & + [\mu(k_j,\omega_j)^2 - 1]\frac{\Omega k_j}{A_j}\left(\frac{d\phi_j}{dy}\right)^2\Big|_{y=l} + \frac{k_jA_j\Delta^2}{\Omega(A_j-n_0)^2}\left(\frac{d\phi_j}{dy}\right)^2\Big|_{y=0}\,, \end{aligned} \tag{37}$$

$$\begin{aligned} C_{\chi,j} = {} & \frac{k_j}{\Omega}\int_0^l v_0\frac{p_j}{A_j}\left[2n_0u_j\left(2\frac{\omega_{e,j}^2}{A_j}+1\right) - 4\Delta^2 n_0\frac{k_jp_j\omega_{e,j}}{\Omega A_j^2} + \frac{k_jp_j}{\omega_{e,j}^2}\frac{dn_0}{dy}\right]dy \\ & + \int_0^l\left[\frac{u_j^2}{k_j}(A_j-n_0) + \frac{k_j}{A_j^2}\left(\frac{2\Delta^2n_0}{\Omega^2} - A_j\right) + \frac{n_0p_ju_j}{\Omega\omega_{e,j}A_j}(A_j-\omega_{e,j}^2)\right]dy \\ & + \frac{1}{A_j}\{\Omega k_jv_0[\mu(k_j,\omega_j,\gamma_j)^2 - 1] + \mu(k_j,\omega_j)(\Omega^2-\omega_{e,j}^2)\}\left(\frac{dp_j}{dy}\right)^2\Big|_{y=l}\,, \end{aligned} \tag{38}$$

$$\begin{aligned} C_{3w,j} = {} & \int_0^l\Bigg\{\left(\frac{p_kp_l}{A_kA_l}\right)^*\left(u_j\omega_{e,j} - \frac{\Delta^2k_jp_j}{\Omega A_j}\right) \\ & \times\left\{2k_kk_l\left[1 - \frac{\Delta^2n_0}{\Omega^2}\left(\frac{1}{A_k^*}+\frac{1}{A_l^*}\right)\right] - \frac{1}{\Omega}\frac{dn_0}{dy}\left(\frac{k_k}{\omega_{e,l}^*}+\frac{k_l}{\omega_{e,k}^*}\right)\right\} \\ & + 2\frac{k_j\Delta^2n_0p_j}{\Omega^2A_j}\left[\left(\frac{k_kp_ku_l}{A_k^2k_l}\right)^*(k_k\omega_{e,k}+k_j\omega_{e,j})^* + \left(\frac{k_lp_lu_k}{A_l^2k_k}\right)^*(k_l\omega_{e,l}^*+k_j\omega_{e,j})\right] \\ & - \frac{k_j^2p_j}{\Omega\omega_{e,j}}\left(\frac{p_ku_l}{k_l\omega_{e,k}}+\frac{p_lu_k}{k_k\omega_{e,l}}\right)^*\frac{dn_0}{dy} + 2u_k^*u_l^*\left(\frac{\Delta^2k_jp_j}{\Omega A_j} - u_j\omega_{e,j}\right)\Bigg\}dy \\ & + \left[i\frac{k_j^2u_k^*u_l^*}{k_kk_l} - ik_j\,\mu(k_j,\omega_j)\left(\frac{u_kk_lp_l}{k_kA_l}+\frac{u_lk_kp_k}{k_lA_k}\right)^*\right]\frac{d\phi_j}{dy}\Big|_{y=l} \\ & - ik_j^2\frac{A_ju_k^*u_l^*}{A_j-n_0}\frac{d\phi_j}{dy}\Big|_{y=0}\,, \end{aligned} \tag{39}$$

where '$*$' indicates the complex conjugate and

$$\mu(k_j,\omega_j) = \frac{d_j\phi_j}{d\phi_j/dy}\Big|_{y=l}\,. \tag{40}$$

The parameter μ is the (complex) ratio of $-iE_x/E_y$ at the tip of the vanes for the jth mode, which may be determined either from the integrated solution or from the model of the slow-wave structure.

Given these coefficients, it is straightforward, for a given k, to use the linear

https://doi.org/10.1017/S0022377800008783 Published online by Cambridge University Press

dispersion relations to obtain the ωs and the γs, numerically solve for the modal functions p, u, and ϕ, and then integrate the above expressions for the three Cs. Of these three Cs, only their ratios are important. The ratio $C_{\chi,j}/C_{\tau,j}$ must be the complex group velocity, $d\omega(k)/dk = d[\omega_r(k) + i\gamma(k)]/dk$ (Kaup and Thomas 1989). The nonlinear coupling coefficient is

$$K_{j,kl} \equiv K(k_j, k_k, k_l) = \frac{C_{3w,j}}{C_{\tau,j}}\,. \tag{41}$$

This coefficient, along with $\delta\omega_r$, determine how rapidly any two modes will parametrically interact, generating the third.

Of all the possible parametric interactions, the most important will be triads containing the RF pump wave, wherein the beating of a noise mode (with wavenumber k_2) against the RF pump (with wavenumber k_1) will generate a daughter mode (with wavenumber $k_3 = -k_1 - k_2$). We assume that the RF pump has saturated. Thus ψ_1 (the RF pump amplitude) is large, and ψ_2 and ψ_3 (the noise modes) are small. Consequently, the RF pump is at its maximum amplitude, is travelling down the slow-wave structure, and is generating the maximum parametric interaction.

To see how the noise modes will grow and evolve, we turn to (35). Let us consider the case where one has spatial uniformity, so that $\partial_\chi \psi_j = 0$. Then (35) reduces to

$$\partial_\tau \psi_2 = -K_{2,13}\psi_1^*\psi_3^* e^{i\delta\omega_r\tau}e^{\delta\gamma_2\tau}\,, \tag{42a}$$

$$\partial_\tau \psi_3 = -K_{3,12}\psi_1^*\psi_2^* e^{i\delta\omega_r\tau}e^{\delta\gamma_3\tau}\,. \tag{42b}$$

(The corresponding equation for the RF pump will give $\partial_\tau\psi_1 = 0$ when ψ_1 and ψ_2 are vanishingly small.) Taking ψ_1 to be constant, these equations form a second-order linear system of ordinary differential equations, for ψ_2 and ψ_3. Since the RF pump has saturated, $\psi_1 e^{\gamma_1 t}$ is at its maximum possible value, and can then to be replaced by the constant saturated value ψ_{1f}. For daughter wavenumbers k_2 and k_3, (42) has the solution

$$\psi_2 = e^{i\delta\omega_r\tau/2}e^{\delta\gamma_2\tau/2}h_2(\tau)\,, \tag{43}$$

where h_2 satisfies the constant-coefficient ordinary differential equation

$$\partial_\tau^2 h_2 - [\tfrac{1}{4}(i\delta\omega_r + \delta\gamma_2)^2 + K_{2,13}K_{3,12}^*|\psi_f|^2]h_2 = 0\,. \tag{44}$$

The important quantity will be the nonlinear parametric growth rate of the jth mode, Γ_j. From (43) and (44), this has two values, given by

$$\Gamma_2 = \tfrac{1}{2}\delta\gamma_2 \pm \Re\big\{[\tfrac{1}{4}(i\delta\omega_r + \delta\gamma_2)^2 + K_{2,13}K_{3,12}^*|\psi_f|^2]^{1/2}\big\}, \tag{45}$$

where $\Re$ indicates the real part. The nonlinear growth rate for the third mode, k_3, is $\Gamma_2 - \delta\gamma_2$.

In Figs. 11(a,b), we have plotted the maximum of the linear growth rate, and also the maximum of the total growth rate (linear plus the nonlinear contribution), for the two daughter waves. As one can see, in some regions, the total growth rate is less than the linear growth rate. This occurs because the nonlinear contribution can oppose the linear growth rate. For the $\omega_0/\Omega = 0.90$ case, between the operating voltages from the Hartree voltage ($V_r = 0.61$) on up to $V_r = 0.70$, the parametric interactions add no significant contribution to the growth rate. However, when the relative voltage has reached $V_r = 0.75$, and definitely by $V_r = 0.78$, the influence of the parametric interactions has very suddenly swelled, and has rapidly became

https://doi.org/10.1017/S0022377800008783 Published online by Cambridge University Press

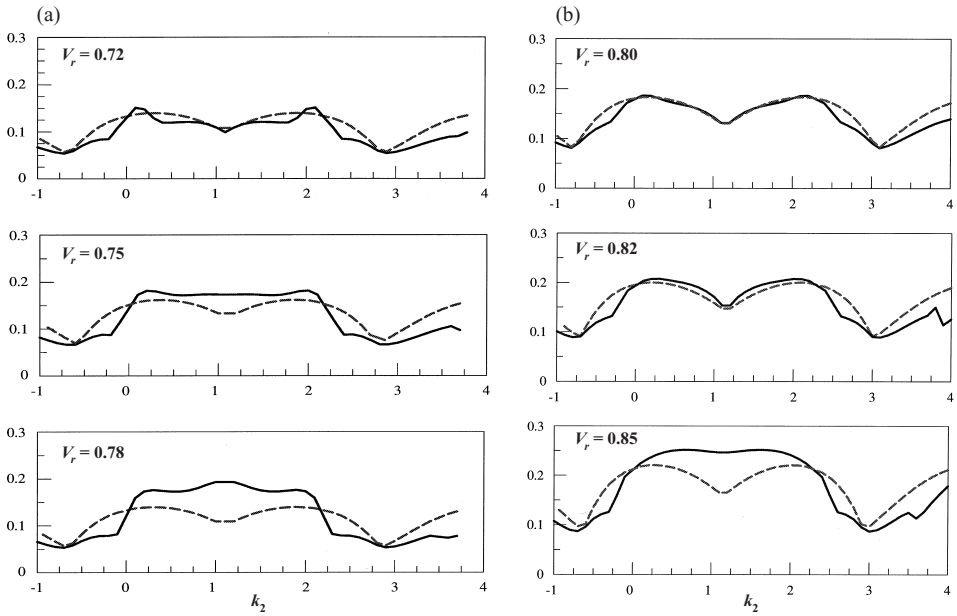


Figure 11. The maximum linear growth rate (dashed curves) and maximum total (linear plus nonlinear) growth rate (full curves) as functions of k at different voltages. (a) is for $\omega_0/\Omega = 0.90$, at the voltages $V_r = 0.72$, 0.75 and 0.78, and (b) is for $\omega_0/\Omega = 1.10$, at the voltages $V_r = 0.80$, 0.82, and 0.85. Note that between $V_r = 0.72$ and $V_r = 0.78$ in (a), the nonlinear contribution has gone from being insignificant to dominant, particularly near the subharmonic ($k_2 = k_3 = -\frac{1}{2}k_1 = 1.1$). The same occurs between $V_r = 0.80$ and $V_r = 0.85$ for $\omega_0/\Omega = 1.10$.

the dominant contribution to the growth rate. The most rapidly growing mode is the subharmonic mode, which is where $k_2 = k_3 = -\frac{1}{2}k_1$.

The reason for the dominance at the subharmonic becomes apparent if we look at Fig. 8. Note that the $\omega_r(k)$ curve is almost a straight line, but with a slight negative curvature, until one is above the RF pump wavenumber, where the curve sharply turns over and flattens out. Consequently, as long as one is below the RF pump's wavenumber, one can find values for k_2 and k_3 that will produce a very near resonance, and thus $\delta\omega_r$ will be small. It happens that at the subharmonic point, $\delta\omega_r$ does take on its smallest value. On the other hand, if either k_2 or k_3 lies above the RF wavenumber, then, since the respective phase velocities diverge even more, $\delta\omega_r$ rapidly increases, which effectively limits the parametric growth.

5. Conclusions

We have shown that an analytical model based on Fourier modes can be used to obtain significant and important information concerning the operation of, and the parameter regimes of, crossed-field devices. The key feature has been to use the second-order nonlinear diffusion equation to define the stationary operating density profiles, which can then be calculated from the nonlinear diffusion coefficient. Such profiles do give us operating curves (Fig. 2) that are in reasonable overall agreement with experimental data. However, an exact comparison is not possible, since these curves are asymptotic limits, and do not take into account the initial growth at the entrance of and in the first part of the device.

https://doi.org/10.1017/S0022377800008783 Published online by Cambridge University Press

Of course, one interest in such a study is to see if the analytical theory could demonstrate any significant differences between the model characteristics for low magnetic fields ($\Omega/\omega_0 \approx 1$), which is the ultralow-noise regime, and those for high magnetic fields ($\Omega/\omega_0 \approx 2$), which is the standard regime for these devices. We have studied this model for a wide variety of possible parameters, and, except for the increased velocities at the cathode, we have not seen any other significant difference between these two regimes that could be related to the ultralow-noise phenomena.

A very significant result of this study has been an explanation for a commonly known experimental fact. This is that almost no device works at an operating voltage more than about 20% above the Hartree voltage (the turn-on voltage), and certainly can never be found to operate near the Hull voltage. As seen in Fig. 7, at 20% above the Hartree voltage ($V_r = 0.61$), parametric interactions suddenly begin to dominate, with the fastest growth rate being found at the subharmonic. In such a case, one would expect the wide band of wavenumbers around the subharmonic to grow and dominate, interfering with the normal operation of the device. We have found that this characteristic behaviour is generic, and does occur at other values of the operating parameters.

Acknowledgements

We thank Professor J. Yang of the University of Vermont for providing an adaptive Runge–Kutta subroutine, on which these calculations were based. This research has been supported in part by the AFOSR and the Naval Surface Warfare Center, Crane Division.

Appendix

In this appendix, we give a brief derivation of the coefficients in the three-wave equation, (35). Using (34), and similar expansions for $\boldsymbol{v}$, and ϕ, one expands the cold-fluid equations, (1)–(3), retaining only the RF terms up to order ϵ^2. Not given in (34) are second-order RF corrections to n, $\boldsymbol{v}$, and ϕ, which must be included. We retain the definitions of v_{1x} and v_{1y} in terms of u and p, as given by (11) and (12), thereby moving any second-order corrections of $\boldsymbol{v}$ into p and u, thereby requiring p and u to contain order-ϵ terms as well. For n_1, ϕ_1, and $\partial_y\phi$, we define them, with their order-ϵ corrections, to be given by

$$n_1 = ip\left(\frac{2kn_0^2}{\Omega A^2} - \frac{\partial_y n_0}{A\omega_e}\right) + \epsilon\delta n_1\,, \tag{A 1}$$

$$\phi_1 = \frac{ip\Delta^2}{Ak\Omega} - \frac{iu\omega_e}{k^2} + \epsilon\delta\phi_1\,, \tag{A 2}$$

$$\partial_y\phi_1 = \frac{i\Omega}{k}u - \frac{i\omega_e}{A}p + \epsilon\delta[\partial_y\phi_1]\,, \tag{A 3}$$

which are the extended forms of (15)–(17). For the first mode, we let S_n, S_x, S_y, and S_ϕ be the respective order-ϵ^2 sources of the respective cold-fluid equations; (1), (2), and (3). These are:

$$\delta n_1 = i\frac{\Delta^2 - \omega_e^2}{\omega_e A}S_n + \frac{n_0}{A}\left[\frac{\Omega}{\omega_e}\left(kS_y + i\partial_y S_x\right) - \partial_y S_y - ikS_x - S_\phi\right]\,, \tag{A 4}$$

$$\delta\phi_1 = \frac{i}{k}S_x\,, \tag{A 5}$$

$$\delta[\partial_y\phi_1] = -S_y\,, \tag{A 6}$$

https://doi.org/10.1017/S0022377800008783 Published online by Cambridge University Press

where it is understood that in this appendix, the values of ω and k are those for the first mode (i.e. $\omega = \omega_1$ and $k = k_1$). The sources are

$$S_n = -i\epsilon p\left(\frac{2kn_0^2}{A^2\Omega} - \frac{\partial_y n_0}{A\omega_e}\right)(\partial_\tau\psi_1 + v_0\partial_\chi\psi_1) - i\epsilon k(n_2^* v_{3x}^* + n_3^* v_{2x}^*)e^{i\delta\omega_r\tau}e^{\delta\gamma_1\tau}\,, \quad (A\,7)$$

$$S_x = -\epsilon\frac{iu}{k}(\partial_\tau\psi_1 + v_0\partial_\chi\psi_1) + i\epsilon\left(\frac{\Delta^2 p}{k\Omega A} - \frac{\omega_e u}{k^2}\right)\partial_y\psi_1 - i\epsilon k v_{2x}^* v_{3x}^*\psi_2^*\psi_3^* e^{i\delta\omega_r\tau}e^{\delta\gamma_1\tau}\,, \quad (A\,8)$$

$$S_y = -\epsilon\frac{p}{A}(\partial_\tau\psi_1 + v_0\partial_\chi\psi_1) + i\epsilon(k_3 v_{2x}^* v_{3y}^* + k_2 v_{3x}^* v_{2y}^*)\psi_2^*\psi_3^* e^{i\delta\omega_r\tau}e^{\delta\gamma_1\tau}, \quad (A\,9)$$

$$S_\phi = 2\epsilon\left(\frac{\Delta^2 p}{\Omega A} - \frac{\omega_e u}{k}\right)\partial_\chi\psi_1\,. \quad (A\,10)$$

One also finds that the equations determining p and u are modified with order-ϵ corrections. Thus (7) and (8) are replaced by

$$\partial_y p = Au + \delta P\,, \quad (A\,11)$$

$$\partial_y u = Bp + \delta U\,, \quad (A\,12)$$

where A and B are still given by (9) and (10), and

$$\psi_1\delta P = \frac{k\Delta^2}{\Omega A}\left(\frac{S_n}{\omega_e} + kS_x - i\partial_y S_y - iS_\phi\right) + \frac{k(n_0 - \omega_e^2)}{\omega_e A}(\partial_y S_x - ikS_y)\,, \quad (A\,13)$$

$$\psi_1\delta U = S_n + \omega_e(kS_x - i\partial_y S_y - iS_\phi) + \Omega(ikS_y - \partial_y S_x)\,. \quad (A\,14)$$

Let p_0 and u_0 be the solution of (7) and (8) and let p and u be the solution of (A 11) and (A 12). Then it follows that

$$\partial_y(p_0 u - u_0 p) = p_0\delta U - u_0\delta P. \quad (A\,15)$$

Integration of (A 15) from the cathode to the anode results in (35). In the process, one has to use the boundary conditions on ϕ_1, (A 2), at the cathode and anode in evaluating the left-hand side.

References

Brillouin, L. 1945 *Phys. Rev.* **67**, 260.
Buneman, O., Levy, R. H. and Linson, L. M. 1966 *J. Appl. Phys.* **37**, 3203.
Davidson, R. C. 1984 *Phys. Fluids* **27**, 1804.
Davidson, R. C. 1985 *Phys. Fluids* **28**, 1937.
Davidson, R. C. and Tang, K. T. *Phys. Fluids* **28**, 1169.
Dombrowski, G. E. 1988 *IEEE Trans. Electron Devices*, **35**, 2060.
Kaup, D. J. and Thomas, G. E. 1989 *Stud. Appl. Math.* **81**, 37 [Erratum **83**, 271 (1990)].
Kaup, D. J. and Thomas, G. E. 1992 *Phys. Fluids* **B4**, 2640.
Kaup, D. J. and Thomas, G. E. 1996 *Phys. Plasmas* **3**, 771.
Kaup, D. J. and Thomas, G. E. 1997 *J. Plasma Phys.* **58**, 145.
Kaup, D. J. and Thomas, G. E. 1998 *J. Plasma Phys.* **59**, 259.
Palevski, A., Bekefi, G. and Drobot, A. 1981 *J. Appl. Phys.* **52**, 4938.
Prasad, S. A., Morales, G. J. and Fried, B. D. 1987 *Phys. Fluids* **30**, 3093.
Riyopoulos, S. 1993 *Phys. Rev.* **E47**, 2839.
Riyopoulos, S. 1996 *Phys. Plasmas* **3**, 1137.

https://doi.org/10.1017/S0022377800008783 Published online by Cambridge University Press